Grid Impedance Detection Based On Complex Coefficient Filter and Full-order Capacitor Current Observer for Three-phase Grid-connected Inverters

Kaixin Wang, Yong Yang, *Senior Member, IEEE*, Mingdi Fan, *Senior Member, IEEE*, Yuhang Tang,
Haoyang Li, Rong Chen, Jiefeng Hu, *Senior Member, IEEE*, Weibo Zeng, *Member, IEEE*,
and Jose Rodriguez, *Life Fellow, IEEE*

***Abstract*—This article proposes a new grid impedance detection method incorporating the complex coefficient filter (CCF) with full-order capacitor current observer for a T-type three-level grid-connected inverter controlled by the inverter output current feedback. Compared with conventional CCF impedance detection algorithms, the proposed method reduces the number of current sensors and detects the grid impedance accurately. First, based on the sampled inverter output current and grid-connected voltage signals, the grid-connected current is estimated. Then, the CCF method is used to extract harmonics from the grid-connected current and voltage signals to calculate the grid impedance. Finally, the correctness of the full-order capacitor current observer is verified by simulation and the feasibility and effectiveness of the proposed algorithm are verified experimentally based on a laboratory prototype.**

***Index Terms*—Complex coefficient filters (CCFs), full-order capacitor current observer, grid impedance detection.**

I. INTRODUCTION

THE massive use of renewable energy sources such as solar and wind power has drawn widespread attention to distributed generation. As an important interface between power sources and the distributed generation systems, the high efficiency and stability of grid-connected inverters have become a research hotspot [1], [2], [3], [4], [5]. With increasing penetration of such distributed energy resources, the impedance value of the electricity grid will change greatly at the point of common connection (PCC), leading to a weak grid situation, which will adversely affect the waveform quality and stable operation of the grid-connected inverters [1], [2], [3], [4], [5], [6], [7], [8], [9].

GB38755-2019 “Guidelines for Safety and Stability of Power System” defines the short-circuit ratio (SCR) for the first time. The smaller the SCR is, the weaker the power grid will be, which in turn, brings in more difficulties in controlling the grid-connected inverters. Therefore, it is very necessary to accurately detect the grid impedance. Under weak grid conditions, the control structure of the grid-connected inverter needs to be adjusted adaptively according to the grid impedance value to ensure the stable and efficient operation of the system.

Existing grid-connected inverter grid impedance detection methods are mainly divided into active detection and passive detection. Passive detection methods do not need to inject disturbances into the system as they detect grid impedance based on the inherent characteristics of the system. Passive detection methods mainly include excitation of *LCL* resonance techniques [10], recursive least squares schemes [11], successive iterative approximation strategies [12], extended Kalman filter [13], etc. Furthermore, Xiangchen et al. [14] propose an impedance detection method based on ripple analysis and the structural characteristics of the dc microgrid system and Liang et al. [15] present a new method of tracking impedance using channel frequency response. Although these methods do not affect the stable operation of the system, they are dependent on existing background distortion signals, and the inherent signal-to-noise ratio of the system is low, resulting in low detection accuracy [16]. Besides, passive detection methods are generally computationally complex and difficult to implement in practical systems.

To overcome the above-mentioned problems for the passive detection methods, different active grid impedance detection algorithms have been presented. Active detection methods need to inject disturbances into the system and extract the corresponding disturbance signals at the PCC to calculate the grid impedance. The types of disturbance injection for grid active detection mainly include *PQ* power disturbance injection, wideband pulse

Manuscript received 11 May 2022; revised 3 August 2022 and 13 September 2022; accepted 14 October 2022. Date of publication 25 October 2022; date of current version 18 November 2022. This work was supported in part by the National Natural Science Foundation of China under Grants 51977136, 51907137, 52007127 and 52277062, in part by the Nature Science Youth Foundation of Jiangsu Province under Grant BK20220499 and in part by Projects FB0008, 1210208 and 1221293. Recommended for publication by Associate Editor H. S. Krishnamoorthy. *(Corresponding authors: Yong Yang; Mingdi Fan.)*

Kaixin Wang, Yong Yang, Mingdi Fan, Yuhang Tang, and Rong Chen are with the School of Rail Transportation, Soochow University, Suzhou 215131, China (e-mail: kxwangwangkx@stu.suda.edu.cn; yangy1981@suda.edu.cn; mdfan@suda.edu.cn; yhtangyhtang@stu.suda.edu.cn; chrong@suda.edu.cn).

Haoyang Li and Weibo Zeng are with the GOODWE Power Supply Technology Co., LTD, Suzhou 215100, China (e-mail: haoyang.li@goodwe.com; weibo.zeng@goodwe.com).

Jiefeng Hu is with the Centre for New Energy Transition Research, and with the Institute of Innovation, Science and Sustainability, Federation University Australia, Mount Helen, VIC 3353, Australia (e-mail: j.hu@federation.edu.au).

Jose Rodriguez is with the Faculty of Engineering, Universidad San Sebastian Santiago, Santiago 8370146, Chile (e-mail: jose.rodriguezp@uss.cl).

Color versions of one or more figures in this article are available at https://doi.org/10.1109/TPEL.2022.3217126.

Digital Object Identifier 10.1109/TPEL.2022.3217126

injection, single harmonic injection and so on. Ciobotaru et al. [17] and Fang et al. [18] detect the grid impedance according to the disturbance variation of *PQ* power, but this method is only suitable for *PQ*-controlled grid-connected inverter systems. Neshvad et al. [19] use wideband pulse injection to detect the grid impedance. The advantage of this method is that it can detect the grid impedance value over a wide spectrum rather than a certain frequency point, but its detection accuracy is low and computational burden is heavy. At present, the most commonly used disturbance injection method is the single harmonic injection [20], [21], [22], [23], [24], [27], [28]. In order to reduce the impact of disturbance injection on the system, Asiminoaei et al. [20] conducted a study on the amplitude, duration and frequency of the injected noncharacteristic harmonic.

Most of the above active detection methods use discrete Fourier transform (DFT) to extract harmonics [20], [21], [22]. However, the mutual interference between the spectrums in practical engineering will affect the detection accuracy. To overcome the limitations of DFT, Alves et al. [23] and [24] propose a transient grid impedance detection method based on continuous wavelet transform (CWT). Nevertheless, this method is not applied in practice due to the complexity of CWT and the high redundancy of information. In recent years, the complex coefficient filter (CCF) method has been applied to electrical engineering gradually. Guo et al. [25] combines CCF with phase-locked loop (PLL) to estimate the fundamental positive and negative sequence information and other harmonic components accurately and rapidly under unbalanced grid voltage conditions. Wu et al. [26] presents a dead-time compensation method based on a modified multiple CCF to optimize the control performance of a permanent magnet synchronous motor. Yang et al. [27] and Guo et al. [28] applied the CCF method to grid impedance detection to extract the noncharacteristic harmonics, which can detect accurately in both ideal and unbalanced grids.

All the above-mentioned grid impedance detection algorithms are required to measure voltage and current at the PCC. Since most inverter control strategies in practical engineering are designed based on the inverter output current rather than the grid current, which means that inverter output current sensors, grid voltage sensors and grid current sensors are all needed if the above-mentioned grid impedance detection algorithms are integrated into the inverter controller. Obviously, the use of additional sensors will increase the volume, cost, and even introduce noise [29]. Therefore, current estimation techniques have been adopted to avoid grid current sensors. According to Kirchhoff's law, the key is to estimate the grid current by subtracting the filter capacitor current from the inverter output current. Now the remaining problem that needs to be answered is how to obtain the capacitor current. Indeed, the direct discrete technique is simple and easy to find the capacitor current. Nevertheless, the differential term will affect the stability of the system. Guzman et al. [30] and Kanieski et al. [31] use Kalman filter method for estimation with good robustness. However, Kalman filter gain is complicated to calculate. Xiao et al. [32] and Yang et al. [33] adopt the sliding-mode estimation method to estimate capacitor currents. Cortes et al. [34] and Miskovic et al. [35] use the Luenberger observer to estimate the capacitor current. Although the current can be estimated, the corresponding sliding-mode parameters and Luenberger matrix are not easy to determine. Zheng et al. [36] use a full-order observer to estimate the capacitor current. This method can achieve high estimation accuracy without degrading system stability or increasing calculation complexity.

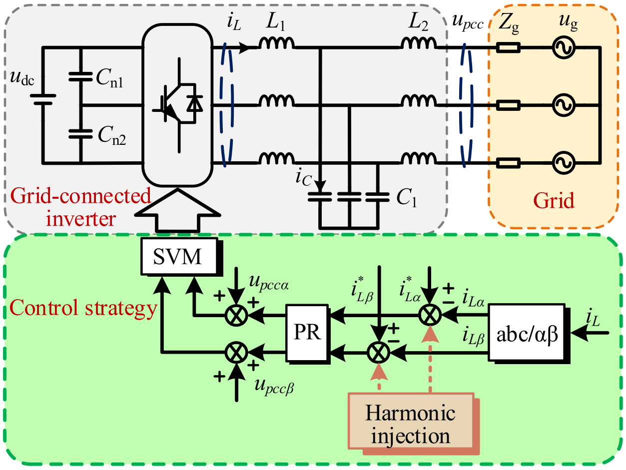

Fig. 1. Conventional control for T-type three-level grid-connected inverters.

To overcome the abovementioned problems, this article proposes a grid impedance detection method incorporating the CCF method with full-order capacitor current observer. Compared with the conventional CCF impedance detection method, it can reduce a capacitor current sensor and accurately detect the grid impedance, reduce the system volume and save cost. Section II introduces the system model of grid-connected inverter and the basic principle of impedance detection based on CCFs; Section III introduces the CCF grid impedance detection method based on the full-order capacitor current observer; the effectiveness of the proposed method is verified by MATLAB/Simulink simulation and experiments in Section IV.

II. SYSTEM MODELING AND PRINCIPLE OF IMPEDANCE DETECTION

A. System Modeling

The block diagram of the control system is shown in Fig. 1 for a T-type three-level grid-connected inverter with *LCL* filter. The control strategy includes current loop PR control and grid-connected voltage feedforward control. In order to suppress *LCL* resonance caused by high impedance, voltage feedforward Lead compensation algorithm is used. The specific control parameters are determined by stability analysis, which is performed by impedance analysis method or small signal model method [37], [38], [39]. When grid impedance detection is required, noncharacteristic current harmonics are injected at the given current.

As shown in Fig. 1, u_{dc} is the dc voltage. C_{n1} and C_{n2} are the bus capacitors. Z_g is the grid impedance. u_g denotes the grid voltage. i_L represents the inverter output current. i_C represents

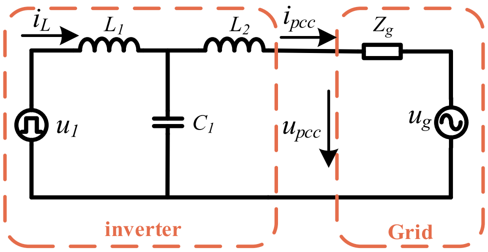

Fig. 2. Simplified model of the grid-connected inverter.

the capacitor current and u_{pcc} represents the grid-connected voltage.

B. Principle of Impedance Detection

The simplified model of the grid-connected inverter is shown in Fig. 2. By injecting noncharacteristic current harmonic disturbance at the given current, the corresponding harmonic response signals $u_{\mathrm{pcc}}(h)$ and $i_{\mathrm{pcc}}(h)$ are extracted for grid impedance detection, where h is the ratio of noncharacteristic harmonic frequency to fundamental frequency (50 Hz).

The specific detection formula is as follows:

$$\overset{\wedge}{Z_g}(h) = \frac{\Delta \hat{u}(h)}{\Delta \hat{i}(h)} = \frac{\overset{\wedge}{u_{\mathrm{pcc}}}(h) - \overset{\wedge}{u_g}(h)}{\overset{\wedge}{i_{\mathrm{pcc}}}(h)} \tag{1}$$

where $\overset{\wedge}{u_g}(h)$ is the noncharacteristic voltage harmonic signal in the power grid, which can be ignored due to its small value compared with $\overset{\wedge}{u_{\mathrm{pcc}}}(h)$. Consequently, (1) can be simplified as

$$\overset{\wedge}{Z_g}(h) = \frac{\overset{\wedge}{u_{\mathrm{pcc}}}(h)}{\overset{\wedge}{i_{\mathrm{pcc}}}(h)} \tag{2}$$

$$\overset{\wedge}{Z_g}(h) = R_g + j\omega L_g. \tag{3}$$

In this article, the correctness of the proposed method is verified under normal grid conditions. It is worth mentioning that when the power grid is polluted, the estimated grid impedance will present fluctuations. To mitigate this problem, we can adjust the amplitude and frequency of the injected harmonics appropriately.

C. Complex Coefficient Filter Harmonic Extraction Method

In this article, the CCF method is used to extract the harmonics of the sampled signals. The first-order complex filter can be expressed as

$$H(s) = \frac{\omega_c}{s - j\omega_0 + \omega_c}. \tag{4}$$

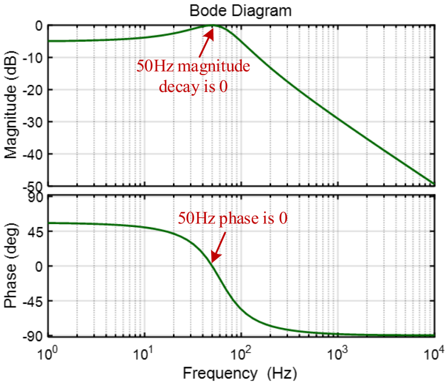

Fig. 3. Bode diagram of first-order CCF.

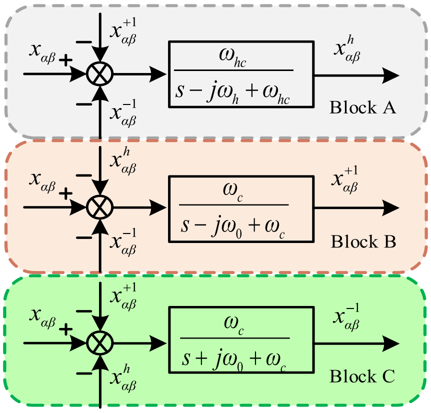

Fig. 4. Schematic illustration of CCF.

The Bode diagram of the first-order CCF is shown in Fig. 3 with $\omega_0 = 314.16$ rad/s and $\omega_c = 221$ rad/s. It can be seen that the first-order CCF can suppress harmonics with ω_c as the cut-off frequency. Compared with a band-pass filter, the complex filter can combine the in-phase and quadrature signals for observation, suppress the negative frequency signals, and retain the positive frequency signals.

Based on the harmonic extraction requirement for grid impedance detection, it is necessary to suppress the positive and negative sequence components of the fundamental frequency signal (there is a negative sequence component when the three-phase grid voltage is unbalanced) and extract the injected noncharacteristic harmonic signal. To meet this requirement, this article adopts the CCF structure diagram designed in Fig. 4.

As shown in Fig. 4, x represents the grid-connected voltage and current signals extracted for grid impedance detection. The CCF control structure includes three parts: block A extracts noncharacteristic signals $x_{\alpha\beta}^{h}$, block B extracts the positive sequence component of the signals $x_{\alpha\beta}^{+1}$, while block C extracts the negative sequence component of the signals $x_{\alpha\beta}^{-1}$.

According to Fig. 4, the transfer function of the noncharacteristic signals extraction can be calculated as

$$H_{\mathrm{CCF}}(s) = \frac{\omega_{hc}\left(s^2 + \omega_0^2\right)}{s^3 + As^2 + Bs + C\omega_0^2} \tag{5}$$

where A $= 2\omega_c$-$j\omega_h$+ω_{hc}, B $= \omega_0^2$-$j2\omega_h\omega_c$, and C $= \omega_{hc}$-$j\omega_h$. ω_0 is the fundamental wave angular frequency; ω_c is the fundamental wave cut-off angular frequency; ω_h is the noncharacteristic harmonic angular frequency; ω_{hc} is the noncharacteristic harmonic cutoff angular frequency.

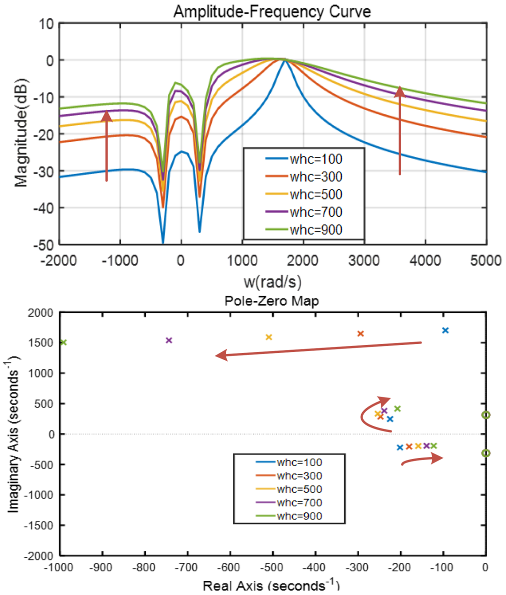

Fig. 5. CCF amplitude-frequency characteristic curve and closed-loop pole distribution diagram when ω_{hc} is different.

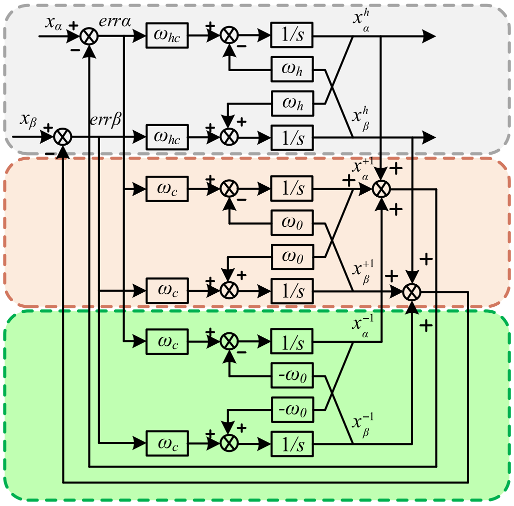

Fig. 6. Coordination transformation for CCF.

Fig. 5 shows the CCF amplitude-frequency characteristic curve and closed-loop pole distribution diagram with $\omega_0 = 314.16$ rad/s, $\omega_c = 221$ rad/s and $\omega_h = 1728$ rad/s when ω_{hc} is different. It can be seen from Fig. 5 that the smaller ω_{hc} is, the higher the detection accuracy will be at the cost of compromising dynamic performance. From this perspective, the parameters should be selected by considering both detection accuracy and dynamic performance comprehensively.

In order to change the complex number j in Fig. 4 into a realizable form, the above principle is implemented in the $\alpha\beta$ coordinate system, where j represents the phase difference between α and β. The transformation process is depicted in Fig. 6.

In practical digital implementation, the control algorithm will be realized and executed in a digital signal processor (DSP). Thus, system models and control signals need to be discretized by Tustin. Taking the α phase noncharacteristic signal as an example, the discretization extraction formula is

$$\left[\mathrm{err}\alpha\left(k\right)\omega_{hc} - x_\beta^h\left(k\right)\omega_h\right]\frac{T_s}{2}\frac{1+z^{-1}}{1-z^{-1}} = x_\alpha^h\left(k\right) \tag{6}$$

$$\begin{aligned} x_\alpha^h\left(k\right) &= x_\alpha^h\left(k-1\right) + \frac{T_s}{2}M\left(k\right) \\ M\left(k\right) &= \left(\mathrm{err}\alpha\left(k\right) + \mathrm{err}\alpha\left(k-1\right)\right)\omega_{hc} \\ &\quad - \left(x_\beta^h\left(k\right) + x_\beta^h\left(k-1\right)\right)\omega_h. \end{aligned} \tag{7}$$

D. Stability Analysis

In order to determine the control parameters of the system, the stability of the current loop is analyzed by impedance analysis method, the specific structural block diagram is shown in Fig. 7.

G_{pll} is the transfer function of the PLL [40], [41]

$$G_{pll} = \frac{1}{2}\frac{k_{p-pll}(s-j\omega_0) + k_{i-pll}}{\left(s-j\omega_0\right)^2 + U_m\left(k_{p-pll}(s-j\omega_0) + k_{i-pll}\right)} \tag{8}$$

where $k_{p\text{-pll}}$ *and* $k_{i\text{-pll}}$ is PI parameter of the PLL, $\omega_0 = 314.16$ rad/s.

Gc is the current loop PR controller

$$G_c = k_p + \frac{2k_r\omega_i s}{s^2 + 2\omega_i s + \omega_0^2} \tag{9}$$

where k_p *and* k_r is PR parameter of the current loop, ω_i is related to the bandwidth of the cut-off frequency.

T_2 is the lead phase compensation

$$T_2 = k_d\frac{sT_d + 1}{s\alpha T_d + 1} \tag{10}$$

where k_d, α, and T_d determine the gain, angle and frequency of compensation.

G_d is the delay link $G_d = e^{-1.5T_s s}$, k_{pwm} is the modulation factor, H_i and H_v is the sampling coefficient.

The output impedance is summarized as formula (11) shown at the bottom of the next page [40]

Bode diagram of the output impedance when PR parameter varies is shown in Fig. 8.

It can be seen from the Fig. 8 that when k_p increases, the amplitude-frequency suppression effect is better and the stability margin increases at high frequencies. Considering the cross-cut frequency and the phase margin at low frequencies, k_p is also going to be large. However, after experimental testing, when k_p is particularly large, *LCL* resonant overcurrent will occur, and active damping cannot suppress the problem. Compared with k_p, the change of k_r has little influence on the stability at high frequencies, so k_r only needs to vary reasonably with k_p.

Based on the above analysis, increasing the k_p and k_r values reasonably is beneficial to the stable operation of the system.

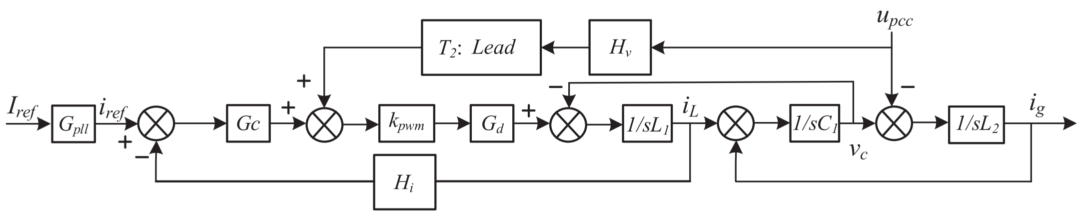

Fig. 7. Structural block diagram of current loop.

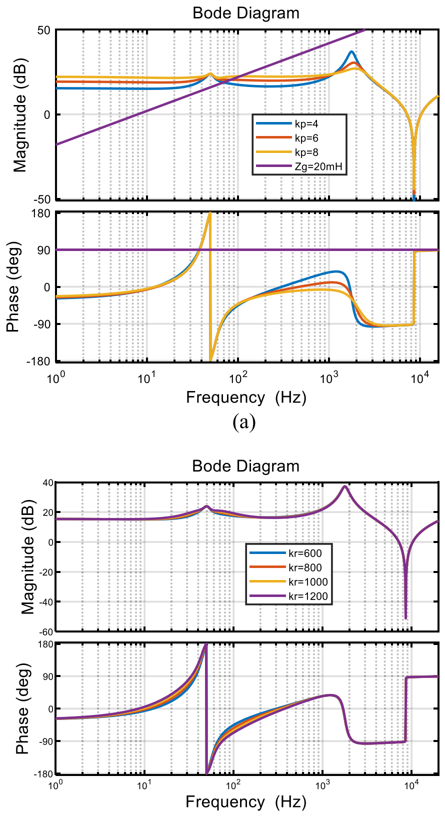

(a)

(b)

Fig. 8. Bode diagram of the output impedance when PR parameter varies. (a) Bode diagram of output impedance as k_p varies. (b) Bode diagram of output impedance as k_r varies.

III. GRID IMPEDANCE DETECTION METHOD COMBINING CCF AND FULL-ORDER CAPACITOR CURRENT OBSERVER

A. Full-order Capacitor Current Observer

According to the analysis in Section II, noncharacteristic grid-connected voltage signal $u_{\mathrm{pcc}}(h)$ and grid-connected current signal $i_{\mathrm{pcc}}(h)$ need to be extracted for grid impedance detection. In order to reduce the use of grid-connected current sensors, the full-order capacitor current observer is employed to observe the capacitor current. Subsequently, the grid current is calculated by the sampled inverter output current and the observed capacitor current.

Since the voltage of the filter inductor L_2 is particularly small compared with the grid-connection voltage, it can be approximated that the sampled grid-connected voltage is equal to the capacitor voltage, namely $u_{\mathrm{pcc}} \approx u_C$, the capacitor current is estimated according to the grid-connected voltage.

Also, since the sampling period is very small compared with the fundamental wave period, it can be assumed that the grid-connected current is constant between two adjacent sampling instants, namely $di_{\mathrm{pcc}}/dt = 0$.

According to the control block diagram in Fig. 1, the following formulas can be obtained:

$$\frac{du_{\mathrm{pcc}}}{dt} = \frac{1}{C_1} i_c \tag{12}$$

$$\frac{di_c}{dt} = \frac{di_L}{dt} - \frac{di_{\mathrm{pcc}}}{dt} = \frac{1}{L_1}\left(u_i - u_{\mathrm{pcc}}\right) \tag{13}$$

where u_i is the output voltage of the inverter, which is replaced by the modulated wave.

The full-order capacitor current observer based on this model structure can be described mathematically as:

$$\frac{d\,\hat{u}_{\mathrm{pcc}}}{dt} = \frac{1}{C_1}\,\hat{i}_c + k_1\left(u_{\mathrm{pcc}} - \hat{u}_{\mathrm{pcc}}\right) \tag{14}$$

$$\frac{d\,\hat{i}_c}{dt} = \frac{1}{L_1}\left(u_i - \hat{u}_{\mathrm{pcc}}\right) + k_2\left(u_{\mathrm{pcc}} - \hat{u}_{\mathrm{pcc}}\right) \tag{15}$$

where $\wedge$ represents the observed value, and k_1 and k_2 are the observation coefficients.

Formula (14) and (15) is discretized to obtain the observed capacitor current:

$$\hat{u}_{\mathrm{pcc}}(k+1) = \hat{u}_{\mathrm{pcc}}(k) + T_s\left(\frac{1}{C_1}\,\hat{i}_c(k) + k_1 e(k)\right) \tag{16}$$

$$\hat{i}_c(k+1) = \hat{i}_c(k) + T_s\left(\frac{1}{L_1}\left(u_i(k) - \hat{u}_{\mathrm{pcc}}(k)\right) + k_2 e(k)\right) \tag{17}$$

where $e(k) = u_{\mathrm{pcc}} - \hat{u}_{\mathrm{pcc}}$ is the voltage observation error, $u_i(k)$ is the voltage modulation wave at the last moment, and the above formula is applicable in the $\alpha\beta$ coordinate system.

$$Z_{0\_\mathrm{pll}} = \frac{s^3 L_1 C_1 L_2 + s^2 C_1 L_2 G_c k_{\mathrm{pwm}} G_d H_i + s\left(L_1 + L_2\right) + G_c k_{\mathrm{pwm}} G_d H_i}{s^2 L_1 C_1 + s C_1 G_c k_{\mathrm{pwm}} G_d H_i + 1 - k_{\mathrm{pwm}} G_d H_v T_2 - G_c k_{\mathrm{pwm}} G_d H_v I_{\mathrm{ref}} G_{\mathrm{pll}}}. \tag{11}$$

B. Determine the Observation Coefficients

In order to determine the observation coefficients k_1 and k_2, the stability analysis of the observer is carried out using the pole placement method. Formula (16) and (17) can be arranged into the following form:

$$\underbrace{\begin{bmatrix}\hat{u}_{\text{pcc}}(k+1)\\ \hat{i}_c(k+1)\end{bmatrix}}_{\hat{x}(k+1)} = \underbrace{\begin{bmatrix}1 & \frac{T_s}{C_1}\\ -\frac{T_s}{L_1} & 1\end{bmatrix}}_{A}\underbrace{\begin{bmatrix}\hat{u}_{\text{pcc}}(k)\\ \hat{i}_c(k)\end{bmatrix}}_{\hat{x}(k)} + \underbrace{\begin{bmatrix}0\\ \frac{T_s}{L_1}\end{bmatrix}}_{B} u_i(k)$$

$$+ \underbrace{\begin{bmatrix}k_1T_s & 0\\ k_2T_s & 0\end{bmatrix}}_{C}\left[x(k)-\hat{x}(k)\right]$$

$$= (A-C)\,x\overset{\wedge}{(k)} + Bu_i(k) + Cx(k) \quad (18)$$

where A, B, and C are the observer coefficient matrices and$x(k) = [\hat{u}_{\text{pcc}}(k)\ \hat{i}_c(k)]^T$.

In order to ensure that the discrete observer is in a stable state, all the eigenvalues of the observer coefficient matrix (*A*–*C*) in the z-plane are required to be in the unit circle, and the characteristic polynomial expression is arranged as follows:

$$\det(zI-A+C) = z^2 + (k_1T_s-2)z + 1 - k_1T_s + \frac{T_s}{C_1}\left(k_2T_s+\frac{T_s}{L_1}\right). \quad (19)$$

Second, in order to achieve a fast dynamic response of the proposed full-order capacitor current observer, the two characteristic values are set to zero to obtain the dead-beat characteristic, namely

$$\det(zI-A+C) = z^2. \quad (20)$$

Comparing formulas (19) and (20), the observation coefficients k_1 and k_2 can be calculated as

$$\begin{cases} k_1T_s - 2 = 0\\ 1 - k_1T_s + \frac{T_s}{C_1}\left(k_2T_s+\frac{T_s}{L_1}\right) = 0\end{cases} \quad (21)$$

$$\begin{cases} k_1 = \frac{2}{T_s}\\ k_2 = \frac{C_1}{T_s^2} - \frac{1}{L_1}\end{cases}. \quad (22)$$

The observed value of capacitor current can be obtained by substituting the observation coefficients into (16) and (17).

C. Grid Impedance Detection Method Combining CCF and Full-order Capacitor Current Observer

In order to save cost and reduce power consumption, this article proposes a grid impedance detection method combining CCF and full-order capacitor current observer. Compared with the conventional CCF impedance detection algorithm, the proposed method reduces the number of current sensors and detects the grid impedance value accurately. The overall control block diagram is shown in Fig. 9.

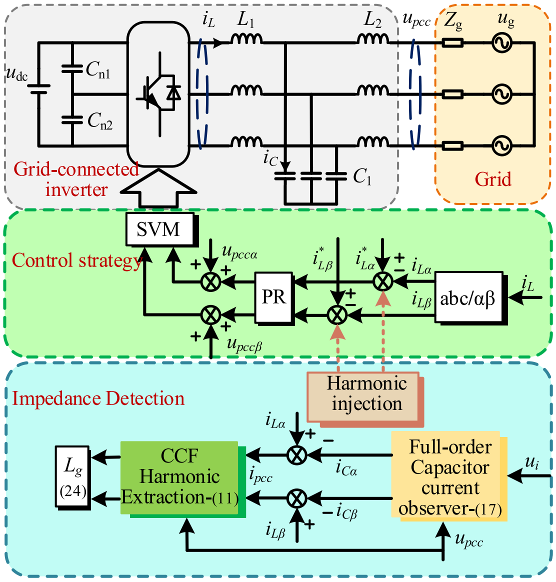

Fig. 9. Overall block diagram of the control system with proposed impedance detection technique.

The overall control system is based on T-type three-level grid-connected inverter with *LCL* filter, and the control system includes inverter control strategy and grid impedance detection. The grid-connected inverter model and control strategy are the same as those introduced in Section II, the grid impedance detection is divided into harmonic injection and harmonic extraction.

Firstly, noncharacteristic harmonic signals are injected at the given current; second, the method proposed in this article calculates the grid-connected current through the sampled inverter output current and the capacitor current estimated by full-order capacitor current observer; then, the grid-connected current signal and the sampled grid-connected voltage signal go through a CCF to extract harmonics; finally, the grid impedance and inductive reactance values are calculated as

$$\begin{aligned} u_{\text{pcc}}(h) &= u_\alpha^h + ju_\beta^h\\ i_{\text{pcc}}(h) &= i_\alpha^h + ji_\beta^h \end{aligned} \quad (23)$$

$$R_g(h) = \text{Re}\left(\frac{u_{\text{pcc}}(h)}{i_{\text{pcc}}(h)}\right) = \frac{u_\alpha^h i_\alpha^h + u_\beta^h i_\beta^h}{i_\alpha^h i_\alpha^h + i_\beta^h i_\beta^h}$$

$$L_g(h) = \text{Im}\left(\frac{u_{\text{pcc}}(h)}{i_{\text{pcc}}(h)}\right) = \frac{u_\beta^h i_\alpha^h - u_\alpha^h i_\beta^h}{i_\alpha^h i_\alpha^h + i_\beta^h i_\beta^h}\frac{1}{\omega_h}. \quad (24)$$

IV. SIMULATION AND EXPERIMENTAL EVALUATIONS

In order to verify the feasibility of the proposed impedance detection method, tests are carried out on MATLAB/Simulink simulation platform and experimental platform. The experimental platform is shown in Fig. 10, which consists of an experimental prototype controlled by a TMS320F28335 DSP, an inductor cabinet, a dc power supply and an ac Source.

The specific experimental parameters are given in Table I.

Appropriate *LCL* filter parameters are selected according to Jiao and Lee [42]. If the injected harmonic amplitude is too large or the injected harmonic frequency is near the fundamental

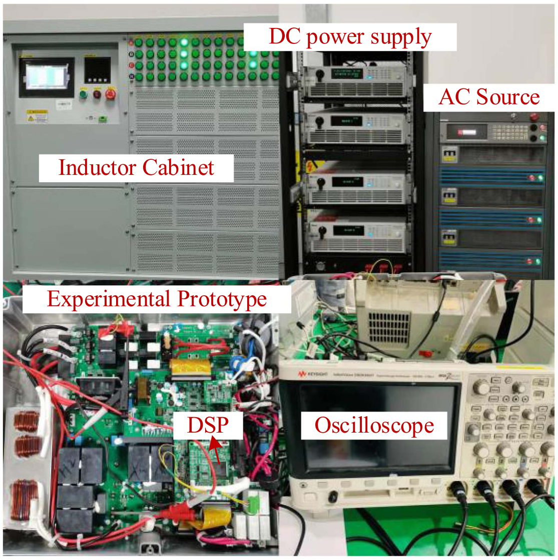

Fig. 10. Experimental platform.

TABLE I
EXPERIMENTAL PARAMETERS

Variable	Description	Unit	Value
u_{dc}	DC-Bus voltage	V	800
f	Base frequency	Hz	50
f_s	Sampling frequency	Hz	16k
L_1	Filter inductance	mH	0.8
C_1	Filter capacitor	μF	7.3
L_2	Filter inductance	mH	0.05
C_{n2} C_{n1}	Balance capacitor	μF	350
u_g	Grid voltage	V	220
ω_h	The angular frequency of inject harmonic	rad/s	1728
ω_{hc}	The cut-off frequency of inject harmonic	rad/s	500
A	Injected harmonic amplitude	A	3

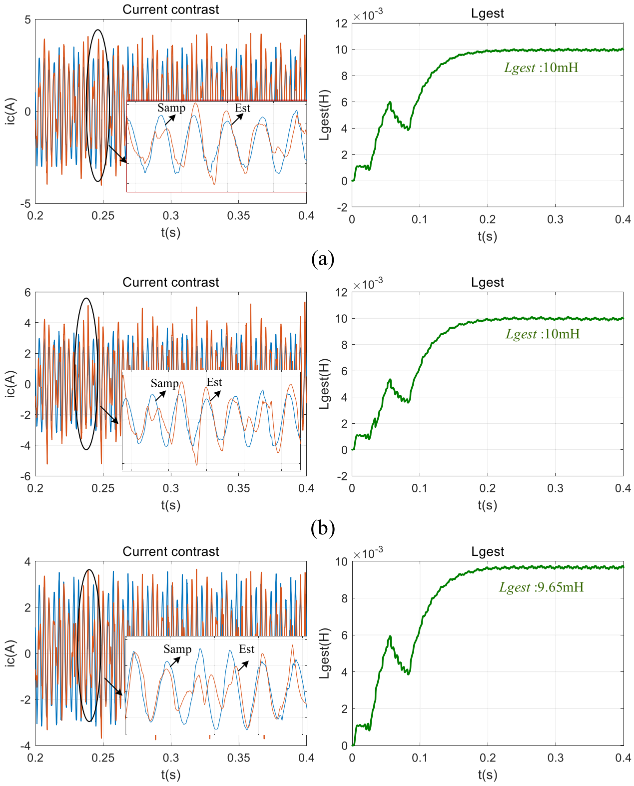

Fig. 11. The results of capacitor current estimation and grid impedance detection. (a) $L_1 = 0.8$ mH $C_1 = 7.3$ μF $L_2 = 0.05$ mH. (b) $L_1 = 0.5$ mH $C_1 = 7.3$ μF $L_2 = 0.05$ mH. (c) $L_1 = 0.8$ mH $C_1 = 5.3\mu$F $L_2 = 0.05$ mH.

frequency, the system stability will deteriorate. By contrast, if the injected harmonic amplitude is too small and the injected harmonic frequency is too high, the detection accuracy will be affected. Usually, the amplitude of the injected harmonic should be 5–15% of the reference current amplitude, and the frequency of the injected harmonic should be 5–15 times of the fundamental frequency [20]. By considering the tradeoff between detection accuracy and system stability, the injected harmonic amplitude and the injected harmonic frequency are set to 3 A and 275 Hz, respectively.

A. *Full-Order Capacitor Current Observation*

To verify the effectiveness of the full-order capacitor current observer, the simulation is carried out on MATLAB/Simulink platform. It is worth noting that *LCL* filter parameters will change during system operation, which may affect the accuracy of capacitor current prediction and impedance detection. Fig. 11 shows the comparison results of the phase-α sampled capacitor current, observed capacitor current and grid impedance detection L_{gest} in different *LCL* filter parameters when the real grid impedance is $Lg = 10$ mH.

It can be seen from Fig. 11 that the following.

1) The observed value of capacitor current basically coincides with the sampled value, which verifies the effectiveness of the capacitor current observation method.
2) The parameter variation of filter capacitor C_1 has an impact on the accuracy of capacitor current estimation and power grid impedance detection, while the parameter variation of filter inductors L_1 and L_2 basically has no impact (the value of L_2 is too small to be ignored).
3) The error of capacitor current estimation has a slight influence on the grid impedance detection result, but it is within the allowable error range.

B. *Simulation Results Under the Polluted Power Grid*

To verify the effectiveness of the proposed grid impedance detection method when the power grid is polluted, the simulation is carried out on MATLAB/Simulink platform. Taking $Lg = 10$ mH as an example, Fig. 12 shows the grid-connected voltage THD and impedance detection results when the different harmonics are injected to the grid.

Through the above tests, it can be seen that when 1% of the fifth and seventh harmonics are injected into the power grid,

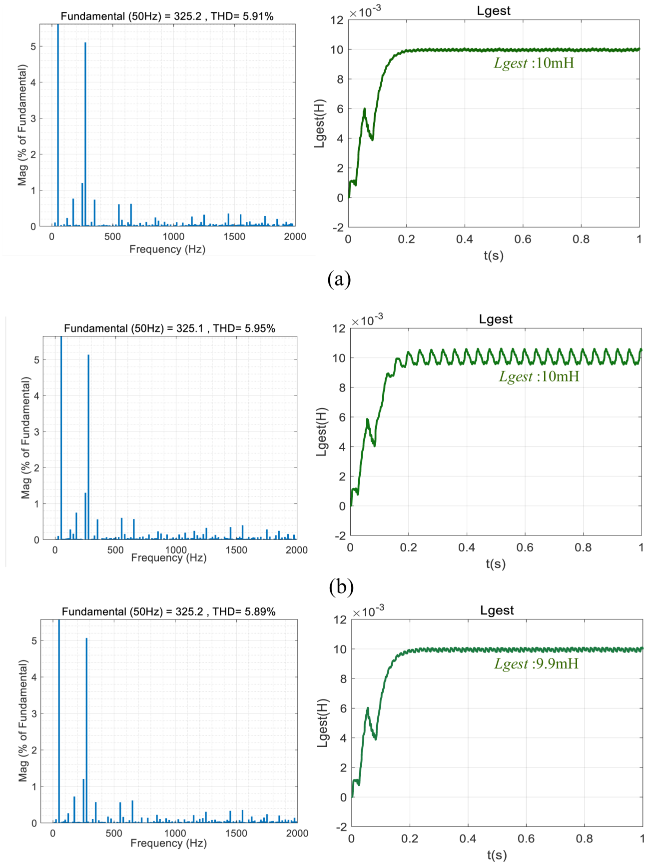

(a)

(b)

(c)

Fig. 12. Impedance detection results when the different harmonics are injected to the grid. (a) Normal grid. (b) 1% of the fifth and seventh harmonics injected to the grid. (c) 1% of the fifth and ninth harmonics are injected to the grid.

the measured impedance values fluctuate slightly around the reference value. When 1% of the seventh and ninth harmonics are injected into the power grid, the measured impedance values do not change obviously. Thus, it is revealed that a polluted power grid can actually deteriorate the impedance detection results to some extent, depending on harmonic distortion frequency. This problem can be alleviated by appropriately adjusting the frequency and amplitude of the injected harmonics.

C. Steady-State Performance

To verify the effectiveness of the proposed grid impedance detection method, steady-state experimental results have been evaluated. The test conditions are set as follows.

1) *Case* A1: The reference of the inverter output current amplitude is set to 2.14 A.
2) *Case* A2: The reference of the inverter output current amplitude is set to 10.7 A.
3) *Case* A3: The reference of the inverter output current amplitude is set to 21.4 A.

Fig. 13 shows experimental results of phase-a grid voltage u_{pa}, phase-a grid current i_{pa}, phase-b grid current i_{pb} and grid impedance detection L_{gest} in case A1. The detected grid

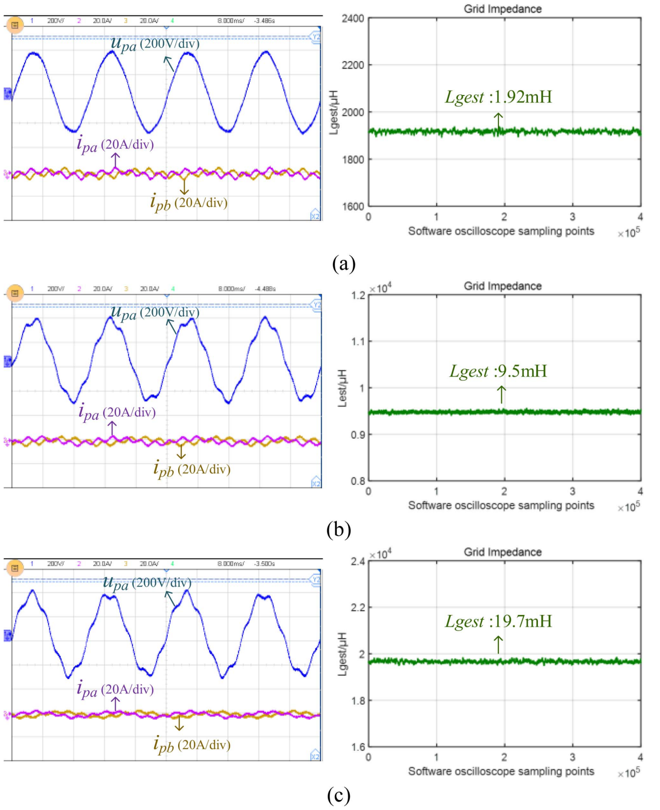

(a)

(b)

(c)

Fig. 13. Steady-state experimental results in case A1. (a) $Lg = 2$ mH. (b) $Lg = 10$ mH. (c) $Lg = 20$ mH.

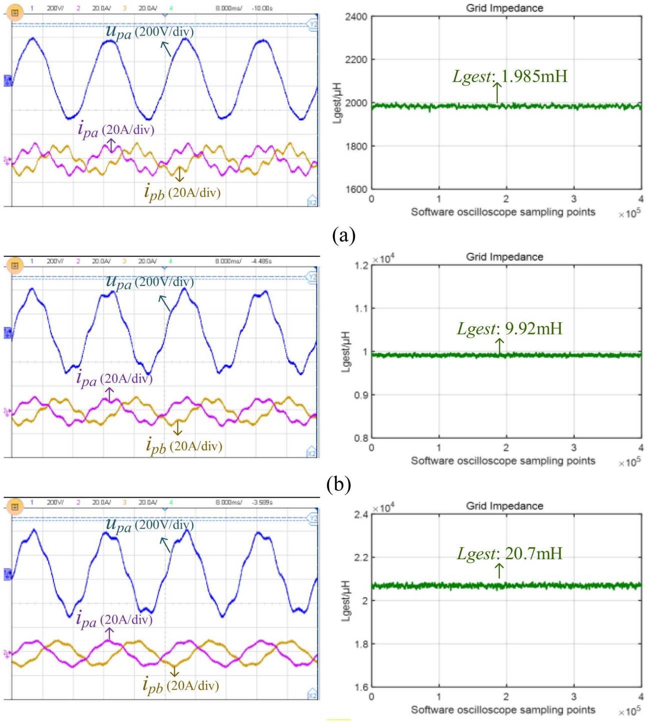

(a)

(b)

(c)

Fig. 14. Steady-state experimental results in case A2. (a) $Lg = 2$ mH. (b) $Lg = 10$ mH. (c) $Lg = 20$ mH.

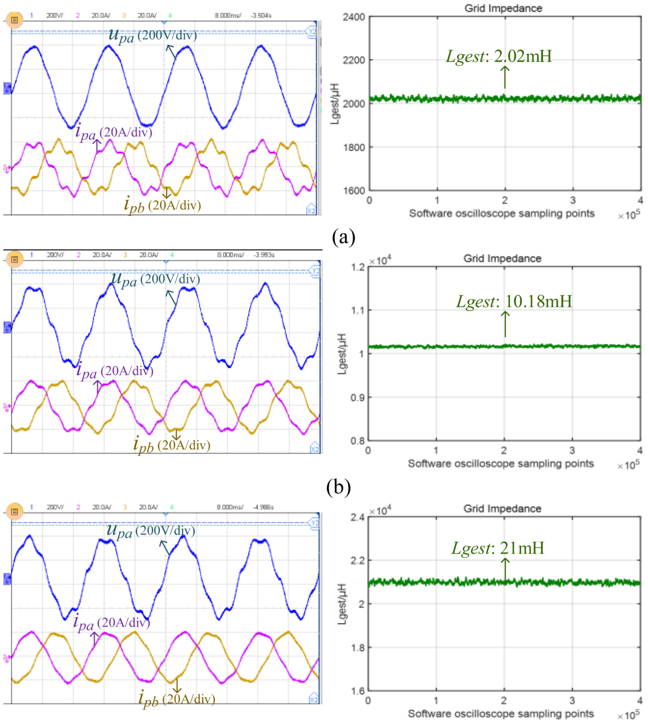

(a)

(b)

(c)

Fig. 15. Steady-state experimental results in case A3. (a) $Lg = 2$ mH. (b) $Lg = 10$ mH. (c) $Lg = 20$ mH.

impedance L_{gest} can be drawn in MATLAB according to the value recorded by the software oscilloscope. As shown in Fig. 13, it can be clearly observed as follows.

1) The detection result is stable at 1.92 mH and the detection error is 4% when the real grid impedance is $Lg = 2$ mH.
2) The detection result is stable at 9.5 mH and the detection error is 5% when the real grid impedance is $Lg = 10$ mH.
3) The detection result is stable at 19.7 mH and the detection error is 1.5% when the real grid impedance is $Lg = 20$ mH. Through the above experiments, it can be seen that the proposed method can accurately detect different impedance values when the three-phase grid-connected inverter is operating at low power, and the detection error is less than 5%.

Fig. 14 shows experimental results of phase-a grid voltage u_{pa}, phase-a grid current i_{pa}, phase-b grid current i_{pb} and grid impedance detection L_{gest} in Case A2. As shown in Fig. 14, it can be clearly observed as

1) The detection result is stable at 1.985 mH and the detection error is 0.75% when the real grid impedance is $Lg = 2$ mH.
2) The detection result is stable at 9.92 mH and the detection error is 0.8% when the real grid impedance is $Lg = 10$mH.
3) The detection result is stable at 20.7 mH and the detection error is 3.5% when the real grid impedance is $Lg = 20$ mH. Through the above experiments, it can be seen that the proposed method can accurately detect different impedance values when the three-phase grid-connected inverter is operating at high power, and the detection error is less than 3.5%.

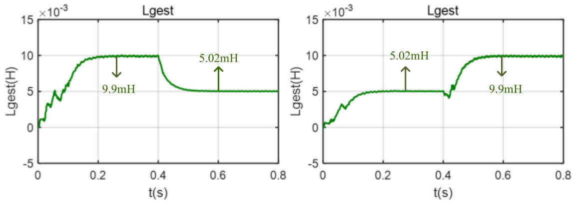

(a) (b)

Fig. 16. Dynamic experimental results. (a) Case B1. (b) Case B2.

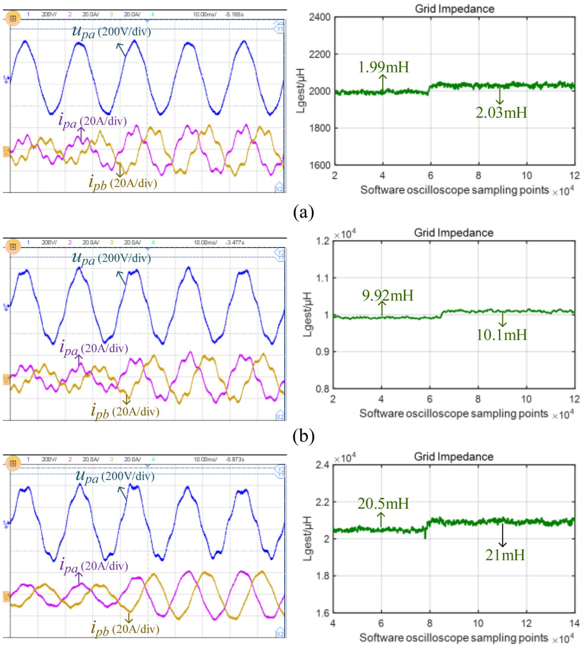

(a)

(b)

(c)

Fig. 17. Impedance detection experimental waveform when the power suddenly increases from 5 to 10 kw. (a) $Lg = 2$ mH. (b) $Lg = 10$ mH. (c) $Lg = 20$ mH.

D. Results of Dynamic Impedance Variations

To verify the effectiveness of the proposed grid impedance detection method, the impedance mutation dynamic experimental is carried out on MATLAB/Simulink platform. The test conditions are set as follows.

1) *Case* B1: The grid impedance value is set from 10 to 5 mh at 0.4 s.
2) *Case* B2: The grid impedance value is set from 5 to 10 mH at 0.4 s.

Fig. 16(a) shows the experimental results in case B1, the detection result is changed from 9.9 to 5.02 mH and the detection error is less than 1%.

Fig. 16(b) shows the experimental results in case B2, the detection result is changed from 5.02 to 9.9 mH and the detection error is less than 1%.

Based on the above two groups of experiments, it is validated that the grid impedance can be accurately estimated when the impedance is changed suddenly, the detection errors are less than 1% and the change times are 0.15 s.

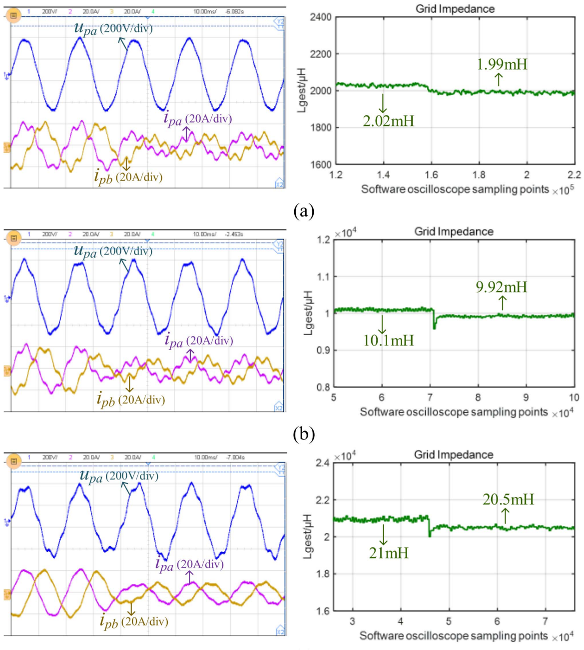

(a)

(b)

(c)

Fig. 18. Impedance detection experimental waveform when the power suddenly drops from 10 to 5 kw. (a) $Lg = 2$ mH. (b) $Lg = 10$ mH. (c) $Lg = 20$ mH.

E. Results of Dynamic Power Output Variations

To verify the effectiveness of the proposed grid impedance detection method, the power mutation dynamic experimental results have been evaluated. The test conditions are set as follows.

1) *Case* C1: The amplitude reference of output currents of three-phase grid-connected inverters is set from 10.7 to 21.4 A.
2) *Case* C2: The amplitude reference of output currents of three-phase grid-connected inverters is set from 21.4 to 10.7 A.

Fig. 17 shows experimental results of phase-a grid voltage u_{pa}, phase-a grid current i_{pa}, phase-b grid current i_{pb} and grid impedance detection L_{gest} in case C1. As shown in Fig. 17, it can be clearly observed the following.

1) The detection result is changed from 1.99 mH to 2.02 mH and the detection error is 1% when the real grid impedance is $Lg = 2$ mH.
2) The detection result is changed from 9.92 mH to 10.1 mH and the detection error is 1% when the real grid impedance is $Lg = 10$ mH.
3) The detection result is changed from 20.5 mH to 21 mH and the detection error is 5% when the real grid impedance is $Lg = 20$ mH.

Through the above experiments, it can be seen that the proposed method can accurately detect different impedance values when the power varies from 5 to 10 kw and the detection error is less than 5%.

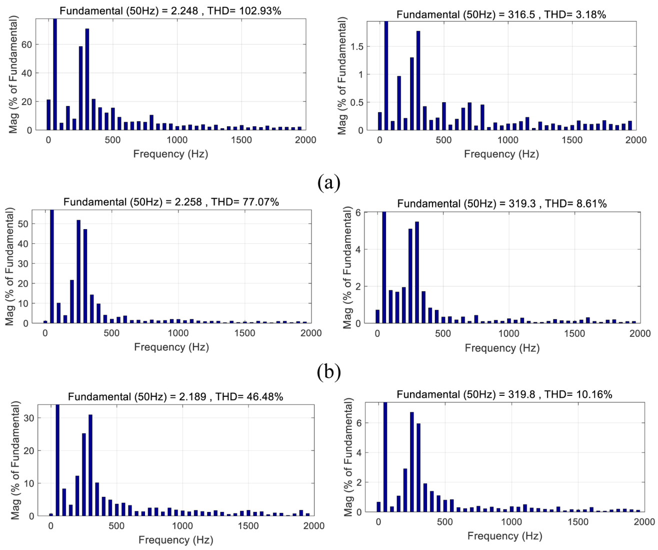

(a)

(b)

(c)

Fig. 19. THD analysis of voltage and current signals in case A1. (a) $Lg = 2$ mH. (b) $Lg = 10$ mH. (c) $Lg = 20$mH.

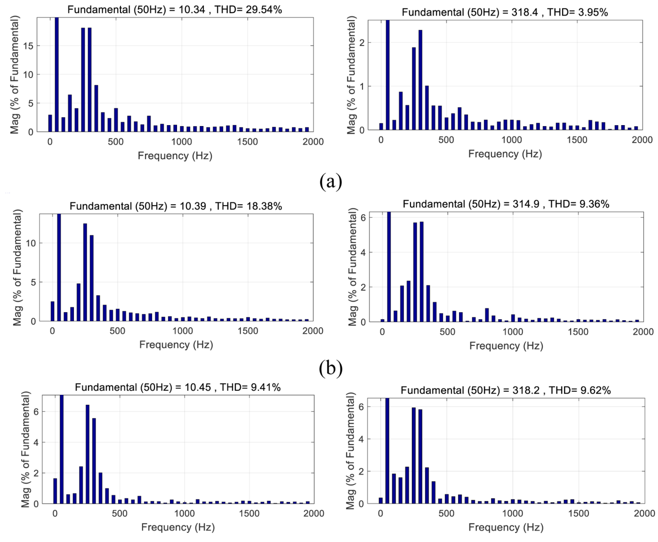

(a)

(b)

(c)

Fig. 20. THD analysis of voltage and current signals in case A2. (a) $Lg = 2$ mH. (b) $Lg = 10$ mH. (c) $Lg = 20$ mH.

Fig. 18 shows experimental results of phase-a grid voltage u_{pa}, phase-a grid current i_{pa}, phase-b grid current i_{pb} and grid impedance detection L_{gest} in Case C2. As shown in Fig. 18, it can be clearly observed as follows.

1) The detection result is changed from 2.02 to 1.99 mH and the detection error is 1% when the real grid impedance is $Lg = 2$ mH.
2) The detection result is changed from 10.1 to 9.92 mH and the detection error is 1% when the real grid impedance is $Lg = 10$ mH.
3) The detection result is changed from 21 to 20.5 mH and the detection error is 5% when the real grid impedance is $Lg = 20$ mH.

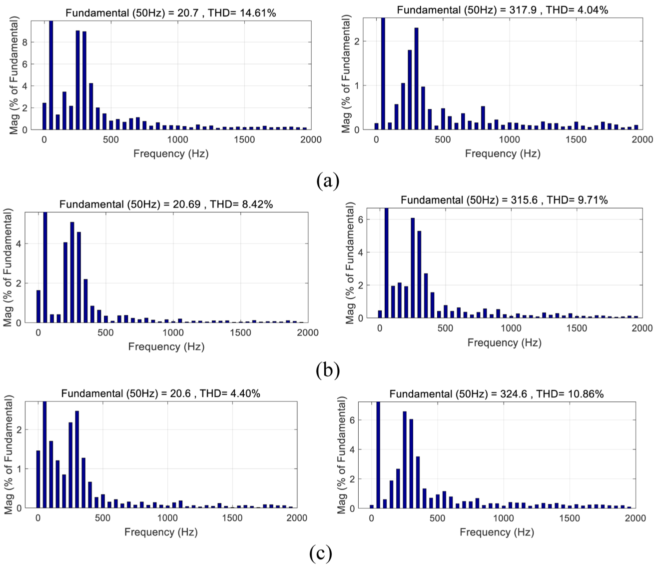

(a)

(b)

(c)

Fig. 21. THD analysis of voltage and current signals in case A3. (a) $Lg = 2$ mH. (b) $Lg = 10$ mH. (c) $Lg = 20$ mH.

Through the above experiments, it can be seen that the proposed method can accurately detect different impedance values when the power is changed from 10 to 5 kw and the detection error is less than 5%.

Based on the above two groups of experiments, it is demonstrated that the grid impedance can be accurately estimated when the inverter output power varies, and detection errors are less than 5%.

It can be seen from the above experimental figure that the greater the power becomes, the greater the estimated grid impedance will be. This may be caused by experimental sampling error, noncharacteristic harmonics content in power grid, LCL filter parameter drift and etc.

F. Total Harmonic Distortion (THD)Analysis of Output Signals

Active detection requires to inject the noncharacteristic harmonics into the system, which will cause distortion of the output signals. Fig. 19 shows the THD analysis of output current and voltage signals in case A1. As shown in Fig. 19, it can be clearly observed that output current THD decreases and output voltage THD increases with the increase of grid impedance under the same power condition.

Fig. 20 shows the THD analysis of output current and voltage signals in case A2. Fig. 21 shows the THD analysis of output current and voltage signals in case A3. Comparing the three groups of figures, it can be seen that the output current THD decreases and the output voltage THD increases with the increase of power under the same impedance condition.

V. CONCLUSION

In this article, a grid impedance detection method incorporating the complex filter method with full-order capacitor current observer is proposed for T-type three-level grid-connected inverter with inverter output current feedback control. The correctness of the full-order current observer is verified in simulations, and then the overall proposed control method is demonstrated in experiments. The results prove that the proposed method can accurately detect the grid impedance with less than 5% detection error under different working conditions. Compared with conventional CCF impedance detection approaches, the proposed method presents distinct advantages such as high accuracy, less number of current sensors required, reduced system cost and volume, as well as reliability against external noises. Since the structure of T-type and pi-type impedance grid is different, the corresponding Kirchhoff law is also different, so the current observation part needs to be remodeled and calculated.

REFERENCES

[1] X. Chen, Y. Zhang, S. Wang, J. Chen, and C. Gong, “Impedance-phased dynamic control method for grid-connected inverters in a weak grid,” *IEEE Trans. Power Electron.,* vol. 32, no. 1, pp. 274–283, Jan. 2017.

[2] Z. Li, J. Hu, and K. W. Chan, “A new current limiting and overload protection scheme for distributed inverters in microgrids under grid faults,” *IEEE Trans. Ind. Appl.,* vol. 57, no. 6, pp. 6362–6374, Nov./Dec. 2021.

[3] Z. Li, K. W. Chan, J. Hu, and J. M. Guerrero, “Adaptive droop control using adaptive virtual impedance for microgrids with variable PV outputs and load demands,” *IEEE Trans. Ind. Electron.,* vol. 68, no. 10, pp. 9630–9640, Oct. 2021.

[4] J. Liu, X. Sun, B. Ren, W. Song, and P. Wheeler, “Strong adaptability control based on dual-division-summation current control for an LCL-Type grid-connected inverter,” *IEEE Trans. Power Electron.*, vol. 37, no. 12, pp. 14157–14172, Dec. 2022.

[5] F. Cecati, R. Zhu, S. Pugliese, M. Liserre, and X. Wang, “State-Feedback reshaping control of voltage source converter,” *IEEE Trans. Power Electron.*, vol. 37, no. 12, pp. 14280–14293, Dec. 2022.

[6] M. Liserre, R. Teodorescu, and F. Blaabjerg, “Stability of photovoltaic and wind turbine grid-connected inverters for a large set of grid impedance values,” *IEEE Trans. Power Electron.*, vol. 21, no. 1, pp. 263–272, Jan. 2006.

[7] X. Lin, J. Yu, R. Yu, J. Zhang, Z. Yan, and H. Wen, “Improving small-signal stability of grid-connected inverter under weak grid by decoupling phase-lock loop and grid impedance,” *IEEE Trans. Ind. Electron.,* vol. 69, no. 7, pp. 7040–7053, Jul. 2022.

[8] J. Xu, S. Xie, Q. Qian, and B. Zhang, “Adaptive feedforward algorithm without grid impedance estimation for inverters to suppress grid current instabilities and harmonics due to grid impedance and grid voltage distortion,” *IEEE Trans. Ind. Electron.,* vol. 64, no. 9, pp. 7574–7586, Sep. 2017.

[9] J. Sun, “Impedance-Based stability criterion for grid-connected inverters,” *IEEE Trans. Power Electron.*, vol. 26, no. 11, pp. 3075–3078, Nov. 2011.

[10] M. Liserre, F. Blaabjerg, and R. Teodorescu, “Grid impedance estimation via excitation of *LCL*-filter resonance,” *IEEE Trans. Ind. Appl.*, vol. 43, no. 5, pp. 1401–1407, Sep./Oct. 2007.

[11] S. Cobreces, P. Rodriguez, D. Pizarro, R. F. Rodriguez, and B. E. Bueno, “Complex-space recursive least squares power system identification,” in *Proc. IEEE Power Electron. Specialists Conf.*, 2007, pp. 2478–2484.

[12] M. Ciobotaru, V. Agelidis, and R. Teodorescu, “Line impedance estimation using model based identification technique,” in *Proc. 14th Eur. Conf. Power Electron. Appl.*, Sep. 2011, pp. 1–9.

[13] N. Hoffmann and F. W. Fuchs, “Minimal invasive equivalent grid impedance estimation in inductive–resistive power networks using extended Kalman filter,” *IEEE Trans. Power Electron.*, vol. 29, no. 2, pp. 631–641, Feb. 2014.

[14] Z. Xiangchen, Z. Guohui, and Z. Jinbin, “Impedance detection based on ripple analysis and current sharing control in DC microgrid,” *IEEE Access,* vol. 8, pp. 43554–43562, Feb. 2020.

[15] D. Liang, H. Guo, and T. Zheng, “Real-time impedance estimation for power line communication,” *IEEE Access,* vol. 7, pp. 88107–88115, Jun. 2019.

[16] A. Ghanem, M. Rashed, M. Sumner, E. M. El-sayes, and I.I. I. Mansy, “Grid impedance estimation for islanding detection and adaptive control of converters,” in *Proc. 8th IET Int. Conf. Power Electron., Mach. Drives*, 2016, pp. 1–6.

[17] M. Ciobotaru, R. Teodorescu, P. Rodriguez, A. Timbus, and F. Blaabjerg, “Online grid impedance estimation for single-phase grid-connected systems using PQ variations,” in *Proc. IEEE Power Electron. Specialists Conf.*, 2007, pp. 2306–2312.

[18] J. Fang, H. Deng, and S. M. Goetz, “Grid impedance estimation through grid-forming power converters,” *IEEE Trans. Power Electron.*, vol. 36, no. 2, pp. 2094–2104, Feb. 2021.

[19] S. Neshvad, S. Chatzinotas, and J. Sachau, “Wideband identification of power network parameters using pseudo-random binary sequences on power inverters,” *IEEE Trans. Smart Grid,* vol. 6, no. 5, pp. 2293–2301, Sep. 2015.

[20] L. Asiminoaei, R. Teodorescu, F. Blaabjerg, and U. Borup, “Implementation and test of an online embedded grid impedance estimation technique for PV inverters,” *IEEE Trans. Ind. Electron.,* vol. 52, no. 4, pp. 1136–1144, Aug. 2005.

[21] L. Asiminoaei, R. Teodorescu, F. Blaabjerg, and U. Borup, “A digital controlled PV-Inverter with grid impedance estimation for ENS detection,” *IEEE Trans. Power Electron.*, vol. 20, no. 6, pp. 1480–1490, Nov. 2005.

[22] A. V. Timbus, R. Teodorescu, F. Blaabjerg, and U. Borup, “Online grid measurement and ENS detection for PV inverter running on highly inductive grid,” *IEEE Power Electron. Lett.,* vol. 2, no. 3, pp. 77–82, Sep. 2004.

[23] D. K. Alves, R. L. D. A. Ribeiro, F. B. Costa, T. D. O. A. Rocha, and J. M. Guerrero, “Wavelet-Based monitor for grid impedance estimation of three-phase networks,” *IEEE Trans. Ind. Electron.,* vol. 68, no. 3, pp. 2564–2574, Mar. 2021.

[24] D. K. Alves, R. L. A. Ribeiro, F. B. Costa, and T. O. A. Rocha, “Real-Time wavelet-based grid impedance estimation method,” *IEEE Trans. Ind. Electron.,* vol. 66, no. 10, pp. 8263–8265, Oct. 2019.

[25] X. Guo, W. Wu, and Z. Chen, “Multiple-Complex coefficient-filter-based phase-locked loop and synchronization technique for three-phase grid-interfaced converters in distributed utility networks,” *IEEE Trans. Ind. Electron.,* vol. 58, no. 4, pp. 1194–1204, Apr. 2011.

[26] Z. Wu et al., “Dead-Time compensation based on a modified multiple complex coefficient filter for permanent magnet synchronous machine drives,” *IEEE Trans. Power Electron.*, vol. 36, no. 11, pp. 12979–12989, Nov. 2021.

[27] Y. Yang, X. Zhang, and M. Li, “Grid impedance detection method under unbalanced and harmonic grid voltage based on multiple complex coefficient filters,” *J. Power Supply*, vol. 16, no. 2, pp. 69–75, Mar. 2018.

[28] L. Guo, C. Zhu, N. Jin, L. Dai, Y. Li, and Y. Sun, “A grid impedance identification method based on complex coefficient filter considering DC offset effects,” in *Proc. 22nd Int. Conf. Elect. Mach. Syst.*, 2019, pp. 1–6.

[29] M. Mehreganfar, M. H. Saeedinia, S. A. Davari, C. Garcia, and J. Rodriguez, “Sensorless predictive control of AFE rectifier with robust adaptive inductance estimation,” *IEEE Trans Ind. Inform.,* vol. 15, no. 6, pp. 3420–3431, Jun. 2019.

[30] R. Guzman, L.G. de Vicuña, J. Morales, M. Castilla, and J. Miret, “Model-Based control for a three-phase shunt active power filter,” *IEEE Trans. Ind. Electron.,* vol. 63, no. 7, pp. 3998–4007, Jul. 2016.

[31] J. M. Kanieski, R. Cardoso, H. Pinheiro, and H. A. Grundling, “Kalman filter-based control system for power quality conditioning devices,” *IEEE Trans. Ind. Electron.,* vol. 60, no. 11, pp. 5214–5227, Nov. 2013.

[32] D. Xiao, K. S. Alam, R. Dutta, and M. F. Rahman, “Reduced-sensors-based predictive controller for LC filtered four-leg inverters,” *IEEE Open J. Ind. Appl.,* vol. 2, no. 5, pp. 301–309, Oct. 2021.

[33] H. Yang, Y. Zhang, J. Liang, J. Gao, P. D. Walker, and N. Zhang, “Sliding-Mode observer based voltage-sensorless model predictive power control of PWM rectifier under unbalanced grid conditions,” *IEEE Trans. Ind. Electron.,* vol. 65, no. 7, pp. 5550–5560, Jul. 2018.

[34] P. Cortes, G. Ortiz, J. I. Yuz, J. Rodriguez, S. Vazquez, and L. G. Franquelo, “Model predictive control of an inverter with output *LC* filter for UPS applications,” *IEEE Trans. Ind. Electron.,* vol. 56, no. 6, pp. 1875–1883, Jun. 2009.

[35] V. Miskovic, V. Blasko, T. M. Jahns, A. H. C. Smith, and C. Romenesko, “Observer-based active damping of LCL resonance in grid-connected voltage source converters,” *IEEE Trans. Ind. Appl.*, vol. 50, no. 6, pp. 3977–3985, Nov./Dec. 2014.

[36] C. Zheng, T. Dragicevic, and F. Blaabjerg, “Current-sensorless finite-set model predictive control for LC-Filtered voltage source inverters,” *IEEE Trans. Power Electron.*, vol. 35, no. 1, pp. 1086–1095, Jan. 2020.

[37] X. Chen, Y. Zhang, S. Wang, J. Chen, and C. Gong, “Impedance-phased dynamic control method for grid-connected inverters in a weak grid,” *IEEE Trans. Power Electron.*, vol. 32, no. 1, pp. 274–283, Jan. 2017.

[38] Y. Han, H. Chen, Z. Li, P. Yang, L. Xu, and J. M. Guerrero, “Stability analysis for the grid-connected single-phase asymmetrical cascaded multilevel inverter with SRF-PI current control under weak grid conditions,” *IEEE Trans. Power Electron.*, vol. 34, no. 3, pp. 2052–2069, Mar. 2019.

[39] M. Cespedes and J. Sun, “Impedance modeling and analysis of grid-connected voltage-source converters,” *IEEE Trans. Power Electron.*, vol. 29, no. 3, pp. 1254–1261, Mar. 2014.

[40] J. Xu, Q. Qian, B. Zhang, and S. Xie, “Harmonics and stability analysis of single-phase grid-connected inverters in distributed power generation systems considering phase-locked loop impact,” *IEEE Trans. Sustain. Energy,* vol. 10, no. 3, pp. 1470–1480, Jul. 2019.

[41] X. Chen, Y. Zhang, S. Wang, J. Chen, and C. Gong, “Impedance-phased dynamic control method for grid-connected inverters in a weak grid,” *IEEE Trans. Power Electron.*, vol. 32, no. 1, pp. 274–283, Jan. 2017.

[42] Y. Jiao and F. C. Lee, “LCL filter design and inductor current ripple analysis for a three-level NPC grid interface converter,” *IEEE Trans. Power Electron.*, vol. 30, no. 9, pp. 4659–4668, Sep. 2015.

Kaixin Wang received the B.S. degree in engineering in 2020 from Soochow University, Suzhou, China, where she is currently working toward the M.S. degree in engineering with the School of Rail Transportation.

Her research interest includes power electronic technology.

Yong Yang (Senior Member, IEEE) received the B.S. degree in automation from Xiangtan University, Xiangtan, China, in 2003, the M.S. degree in electrical engineering from Guizhou University, Guiyang, China, in 2006, and the Ph.D. degree in electrical engineering from Shanghai University, Shanghai, China, in 2010.

He is currently a Full Professor with the School of Rail Transportation, Soochow University. From December 2017 to December 2018, he was a Visiting Scholar with Center for High Performance Power Electronics, The Ohio State University, Columbus, OH, USA. He has coauthored more than 80 journal and conference papers. His current research interests include model predictive control in power electronic converters, distributed energy resource interfacing and high-performance motor drive control.

Mingdi Fan (Senior Member, IEEE) received the B.S. degree in electrical engineering and the Ph.D. degree in detection technology and automation device from Northwestern Polytechnical University, Xi’an, China, in 2008 and 2014.

From 2010 to 2011, he was a Visiting Scholar with Kassel University. He is currently an Associate Professor with the School of Rail Transportation, Soochow University. His current research interests include model predictive control for power converters and motor drives.

Yuhang Tang received the B.S. degree in engineering in 2020 from Soochow University, Suzhou, China, where he is currently working toward the M.S. degree in engineering with the School of Rail Transportation.

His research interest includes power electronic technology.

Haoyang Li received the B.S. degree in electric engineering and the M.S. and Ph.D. degree in power electronics and power drives from Dalian University of Technology, Dalian, China, in 2008, 2014, and 2019, respectively.

From 2019 to 2020, he was a Lecturer with Shenyang Institute of Engineering. He is currently the Technical Manager with Goodwe Power Technology Co., Ltd., Suzhou, China. His current research interests include developing advanced control algorithms for grid-connected photovoltaic inverters.

Rong Chen was born in Jiangsu, China, in 1983. She received the B.S. degree in communication engineering, the M.S. degree in communication and information system and the Ph.D. degree in signal and information processing from Soochow University, Suzhou, China, in 2006, 2009, and 2013, respectively.

She is currently a Lecturer with the School of Rail Transportation, Soochow University. Her research interests include signal processing and synchronous phasor measuring.

Jiefeng Hu (Senior Member, IEEE) received the Ph.D. degree in electrical engineering from University of Technology Sydney (UTS), Ultimo, NSW, Australia, in 2013.

He participated in the research of minigrids in Commonwealth Scientific and Industrial Research Organization, Newcastle, Australia. He was an Assistant Professor with The Hong Kong Polytechnic University, Hong Kong. He is currently an Associate Professor and a Program Coordinator of Electrical Engineering with Federation University Australia, Ballarat, VIC, Australia, where he is also the Stream Leader of Centre for New Energy Transition Research. His research interests include power electronics, renewable energy, and smart microgrids.

Dr. Hu is an Associate Editor for *IET Renewable Power Generation*, an Editor for IEEE TRANSACTIONS ON ENERGY CONVERSION, an Associate Editor for IEEE ACCESS, and was a Guest Editor for IEEE TRANSACTIONS ON INDUSTRIAL ELECTRONICS for a Special Issue “Applications of Predictive Control in Microgrids.”

Weibo Zeng (Member, IEEE) received the B.S. degree in automation from Jiangxi University of Science and Technology, Ganzhou, China, in 2010.

Since 2013, he has been a Senior Software Engineer with Goodwe Power Technology Co., Ltd., Suzhou, China. His research interests include control of solar inverter and solar power system.

Jose Rodriguez (Life Fellow, IEEE) received the Engineer degree in electrical engineering from the Universidad Tecnica Federico Santa Maria, in Valparaiso, Chile, in 1977 and the Dr.-Ing. degree in electrical engineering from the University of Erlangen, Erlangen, Germany, in 1985.

Since 1977, he has been with the Department of Electronics Engineering, Universidad Tecnica Federico Santa Maria, where he was a full Professor and the President. From 2015 to 2019. he was the President of Universidad Andres Bello in Santiago, Chile. Since 2022, he has been the President of Universidad San Sebastian in Santiago, Chile. He has coauthored two books, several book chapters and more than 700 journal and conference papers. His main research interests include multilevel inverters, new converter topologies, control of power converters, and adjustable-speed drives.

Dr. Rodriguez was the recipient of number of best paper awards from journals of the IEEE He is s member of the Chilean Academy of Engineering. In 2014, he was the recipient of the National Award of Applied Sciences and Technology from the government of Chile and the Eugene Mittelmann Award from the Industrial Electronics Society of the IEEE in 2015. From 2014 to 2021, he has been included in the list of Highly Cited Researchers published by Web of Science.